Dynamics of Photocarrier Separation in MAPbI$_3$ Perovskite Multigrain Films under a Quasistatic Electric Field

Arun Aby Paraecattil,[†] Jelissa De Jonghe-Risse,[†] Vytenis Pranculis,[†,‡] Joël Teuscher,[†] and Jacques-E. Moser[*,†]

[†]Photochemical Dynamics Group, Institute of Chemical Sciences & Engineering, and Lausanne Centre for Ultrafast Science (LACUS), École Polytechnique Fédérale de Lausanne, CH-1015 Lausanne, Switzerland

[‡]Department of Molecular Compounds Physics, Center for Physical Sciences and Technology, 01108 Vilnius, Lithuania

S *Supporting Information*

ABSTRACT: Applying time-resolved electroabsorption spectroscopy for the first time to methylammonium lead triiodide perovskite (MAPbI$_3$) thin films under reverse bias, we monitored optically the ultrafast evolution of the local counter-electric field produced by the drift of photogenerated electrons and holes in opposite directions. Under an externally applied electric field of $|E| < 10^5$ V cm^{-1}, the carriers were found to reach a separation of 40 nm within ~1 ps. This distance corresponds to the average dimensions of crystalline grains in the active film, at the boundaries of which charges were trapped. An intragrain average carrier drift mobility of $\mu_{\pm} = 23$ cm^2 V^{-1} s^{-1} was inferred. Subsequent charge detrapping, migration through the entire film, and accumulation at its insulated surfaces caused a blue shift of the perovskite absorption edge that arose within tens of picoseconds, owing to a trap-limited electron drift mobility $\mu_n = 6$ cm^2 V^{-1} s^{-1}. Charge recombination was entirely suppressed between field-separated photocarriers generated at initial densities of $n_0 \leq 2 \times 10^{16}$ cm^{-3}. Accumulation of electrons at the interface between a mesoporous TiO$_2$ electron-transport layer and a multigrain MAPbI$_3$ film was also observed, which was indicative of delayed charge injection through a poor contact junction.
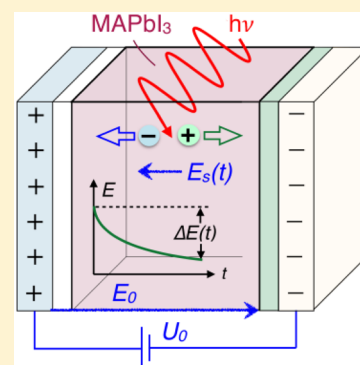
INTRODUCTION

Since their initial demonstration, hybrid organic−inorganic lead trihalide perovskites (APbX$_3$), such as methylammonium lead triiodide (MAPbI$_3$), have proven to be extraordinary materials for photovoltaic and electronic applications.[1−4] Record power conversion efficiencies now exceeding 22% have been achieved with single-junction perovskite solar cells,[5] and devices with a range of architectures and material compositions have been reported.[2,5−9] Spectrally broad, direct-band-gap absorption enables perovskite semiconductor thin films to efficiently harness the solar spectrum. In addition, long carrier diffusion distances and ambipolar charge transport allow for the effective extraction of photogenerated electrons and holes prior to carrier recombination.[10−13] Recent substantial improvements in the stability of perovskite solar cells through various strategies show that this type of photovoltaic converter is becoming close to practical use.[5,14−16]

Despite this very rapid progress, much remains to be understood regarding the intrinsic properties of the materials and the basic mechanisms of solar cell operation. Typical photovoltaic device characterization protocols rely on current−voltage scans to measure power conversion efficiencies. For a number of photovoltaic cell architectures, however, accurate device characterization has proven to be difficult, because of the apparent huge dielectric constant of the perovskite at low frequencies and an anomalous photocurrent hysteresis observed under typical measurement conditions.[17−20] The latter properties reflect a polarization of the active material subjected to an electric field and is believed to be primarily caused by the slow migration of halide ions and halide vacancies within the material and charge accumulation at ion-blocking interfaces.[20−23]

Ionic disorder in iodoplumbate perovskites at room temperature implies the presence of interstitial iodide anions and iodide vacancies within the crystal that are likely to act as hole and electron traps, respectively.[24−26] Photophysical studies,[27−30] photoluminescence nanoimaging,[31] and transient absorption microscopy[32−34] have also evidenced trap and midgap states in the material, which are located predominantly at grain boundaries and interfaces. The size of the crystalline grains in perovskite films and the quality of the electronic contact at the interfaces between the active layer and the electron-donor and -acceptor materials appear, therefore, to play a crucial role in determining the photovoltaic performances of devices.[12,35−37] The design of new possibilities for improving these characteristics call for a deeper insight into the details of the trapping of photogenerated carriers at grain boundaries and of the accumulation of charges at the perovskite interfaces. The determination of carrier mobilities has been achieved so far by the application of various techniques, among

which contactless time-domain terahertz spectroscopy has been one of the favorites. This technique, however, probes the oscillation of carriers over very short distances and hardly allows for the characterization of drift mobilities on the order of 200−400 nm, corresponding to typical thicknesses of perovskite films in a solar cell. Apart from Hall effect measurements, a number of electrical methods, such as time-of-flight (TOF) techniques, have been employed to determine dc mobilities within large crystals and in complete photovoltaic devices.[38,39] The nanosecond time resolution of photocurrent probing constitutes a serious limitation in these cases and prevents the observation of ultrafast stages of the carrier separation dynamics.

Time-resolved electroabsorption spectroscopy (TREAS) has been designed to probe optically the perturbation of an externally applied electric field experienced by an absorber semiconductor, a donor−acceptor bilayer, or a solid blend with femtosecond time resolution.[40] This recently established experimental technique relies on the electric-field-dependent optical response of a material (electroabsorption: Stark or Franz−Keldysh effects). Photogeneration of charge pairs, splitting of these pairs, and subsequent drift of the carriers perturb the electric field exerted locally on the material, causing changes in its absorption or reflectivity. Monitoring the temporal evolution of these optical properties in an ultrafast pump−probe spectroscopy scheme allows for the reconstruction of the electric field and, hence, the dynamics of charge motion. TREAS based on the transient Stark effect has been successfully applied to scrutinize the charge generation and separation dynamics in bilayer and bulk heterojunction organic photovoltaic cells.[41−43] This powerful technique was applied in this work for the first time to investigate the dynamics of charge carrier separation and trapping in MAPbI$_3$ perovskite thin films subjected to an external quasistatic electric field.

■ RESULTS AND DISCUSSION

Thin films of vapor-deposited MAPbI$_3$ were studied using ultrafast time-resolved electroabsorption spectroscopy. This technique involves subjecting the material to a modulated external electric field generated by applying a square-pulse voltage between two electrodes situated on the two sides of the perovskite film. The samples used in this work had a multilayer structure of the form ITO|Al$_2$O$_3$|MAPbI$_3$|poly(methyl methacrylate) (PMMA)|Au, where the active material was sandwiched between two insulating layers acting as barriers against carrier injection and collection at the electrodes. Samples were prepared by coating an ITO/glass conductive transparent substrate with an insulating, 30-nm-thick Al$_2$O$_3$ layer, on top of which a 280-nm-thick film of MAPbI$_3$ was deposited by coevaporation of methylammonium iodide (CH$_3$NH$_3$I) and lead iodide (PbI$_2$).[7,44] An insulating layer of poly(methyl methacrylate) (PMMA) was deposited by spin-coating a solution of the polymer onto the perovskite, allowing the active film to be encapsulated and protected against possible degradation by moisture and oxygen. An 80-nm-thick gold (Au) film was finally vacuum-coated on the PMMA surface. The overall thickness of the sample between the two conductive electrodes was determined by scanning electron microscopy to be 340 ± 20 nm (Figure 1).

After a monochromatic pump pulse (45-fs pulse duration) had photoexcited the MAPBbI$_3$ perovskite absorber, the time evolution of the electric field experienced by the material was measured by monitoring its transient absorption spectra near
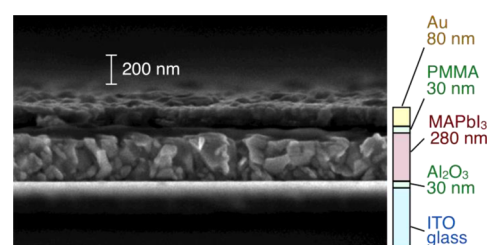

Figure 1. Cross-sectional scanning electron microscopy (SEM) image of an insulated, vapor-deposited MAPbI$_3$ film sandwiched between two conductive electrodes. From bottom to top, the micrograph shows ITO conductive glass coated with an insulating layer of alumina, the perovskite film, a second insulating layer made of spin-coated PMMA, and an evaporated gold layer constituting the second electrode. The polycrystalline morphology of the vapor-deposited MAPbI$_3$ film is clearly visible, with grain size varying between 20 and 150 nm.

the absorption edge using white-light continuum probe pulses delayed by up to 1200 ps with respect to the pump excitation. Figure 2 shows the static electroabsorption (EA) spectrum of
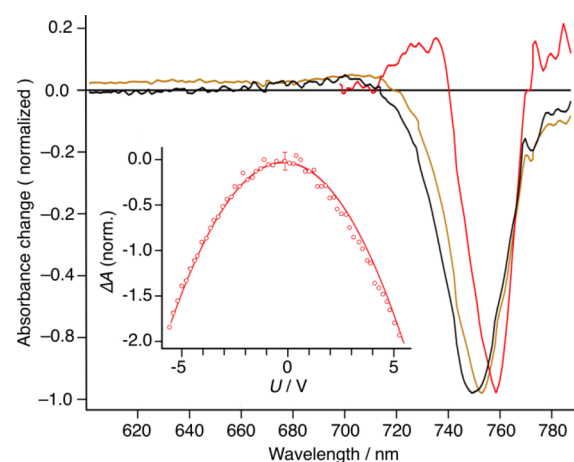

Figure 2. Differential absorption spectra of insulated MAPbI$_3$ films. Yellow line: Transient absorbance (TA) spectrum (U = 0, λ_{pump} = 545 nm, probed 300 ps after pump excitation). Red line: Electroabsorption (EA) spectrum (U = 6.0 V, no pump pulse). Black line: Electromodulated differential absorbance (EDA) spectrum (U = 6.0 V, λ_{pump} = 545 nm, probed 300 ps after pump excitation). Inset: Dependence of the differential electroabsorption (EA) signal measured at λ_{probe} = 762 nm upon the applied voltage (forward and reverse bias). The red curve drawn through the experimental points is the best fit to a parabolic function.

MAPbI$_3$, its transient absorption (TA) spectrum, and its electromodulated differential absorption (EDA) spectrum. The absorbance changes, ΔA, determined in each case are defined by the following differences

EA spectrum

$$\Delta A(\lambda) = A_E(\lambda) - A(\lambda) \tag{1}$$

TA spectrum

$$\Delta A(t, \lambda) = A_{pump}(t, \lambda) - A(t, \lambda) \tag{2}$$

EDA spectrum

$$\Delta A(t, \lambda) = A_{E+pump}(t, \lambda) - A_{pump}(t, \lambda) \tag{3}$$

where $A(\lambda)$ is the absorbance spectrum measured in the absence of a field and with no pump excitation, $A_E(\lambda)$ is the spectrum of the sample subjected to the electric field **E**, $A_{pump}(t, \lambda)$ is the transient spectrum obtained upon laser-pulsed excitation, and $A_{E+pump}(t, \lambda)$ is the transient spectrum of the sample subjected to both the external electric field and the optical pump.

To generate the EA and EDA spectra, a square-pulse voltage was applied between the ITO and Au electrodes with a pulse duration of 100 μs and a repetition rate of 1 kHz. Taking into account the permittivity of the MAPbI$_3$ film as well as those of the two insulating layers, the magnitude of the electric field experienced by the perovskite material was calculated to be $|E|_0 = 0.437U/d$, where U is the voltage applied between the ITO and gold electrodes and $d = 280 \pm 20$ nm is the perovskite film thickness. A voltage of $U = 6.0$ V applied across the whole device hence corresponds to an electric field intensity of $|E|_0 = 9.4 \pm 0.8 \times 10^4$ V cm^{-1} [see the Supporting Information (SI) for details and additional references].

The change in the absorption band shape, $\Delta A(\nu)$, of molecular and excitonic species subjected to an electric field **E** can be described as the sum of first and second derivatives of the absorption spectrum $A(\nu)$[45,46]

$$\Delta A(\nu) = -|E| \frac{\partial A(\nu)}{\partial \nu} \Delta p + \frac{|E|^2}{2} \frac{\partial^2 A(\nu)}{\partial \nu^2} \Delta p^2$$
$$- \frac{|E|^2}{2} \frac{\partial A(\nu)}{\partial \nu} \Delta \alpha \qquad (4)$$

where $|E|$ is the modulus of the electric field exerted on the sample, Δp is the change in permanent dipole moment, and $\Delta \alpha$ is the difference in polarizability between the ground and excited electronic states connected by the optical transition that is being probed. The first term in eq 4 is linear in $|E|$ and reaches zero for isotropic samples, because the transient dipole moment, Δp, is averaged over all possible orientations. The second term shows that changes in the dipole moment are associated with the second derivative of the absorption spectrum, and the last term includes the product of the change in polarizability, $\Delta \alpha$, and the first derivative of the absorption spectrum. The last two terms are quadratic in the field.

The linear and quadratic terms in eq 4 can be distinguished by measuring the electroabsorption as a function of the applied bias voltage. The inset of Figure 2 shows the field dependence of the change in electroabsorption amplitude at the wavelength $\lambda_{probe} = 762$ nm. A parabolic dependence of the EA signal on the applied voltage is observed. In our case, EA measured at the absorption edge seems to be primarily due to a shift and broadening of the Gaussian excitonic band component of the perovskite absorbance spectrum (Figure S1), which is expected to produce a quadratic Stark effect if no permanent dipole moment is effective and the polarizability of the material is reasonably isotropic.[45,46] Electroabsorption spectra of insulated MAPbI$_3$ films were recently shown to also be compatible with a third-order nonlinear optical response and the low-field Franz−Keldysh−Aspnes (FKA) model, according to which relative transmittance or reflectance changes also scale quadratically with the electric field.[47]

The symmetrical responses of the EA signals observed at both forward and reverse applied biases confirm that the insulating layers effectively prevent carrier injection at the electrodes. Any interfacial charge transfer occurring at a particular junction would, indeed, produce a decrease of the

effective electric field exerted on the material and dramatically reduce the observed electroabsorption upon reaching a critical voltage value under normal bias. It also indicates that, if ion migration is induced by the applied electric field, causing a change in the absorption of the material, this must take place on a time scale that exceeds the 100-μs period during which the electric field is applied to the sample.

The EA spectrum in Figure 2 shows a negative absorbance change at $\lambda_{probe} = 745-775$ nm, with a maximum at 762 nm along with a weaker positive ΔA feature at $\lambda_{probe} = 718-745$ nm. An additional positive band above 775 nm cannot be completely resolved because of its overlap with the fundamental emission of the laser. The shape of the EA spectrum is indicative of a blue shift of the excitonic band of MAPbI$_3$ upon application of the external electric field and is typical of quadratic Stark or FKA effects, where the differential absorbance appears as a mixture of the first and second derivatives of the absorption spectrum. The TA spectrum recorded at a delay time of 300 ps after the pump excitation shows a negative band between 720 and 780 nm with a peak at 757 nm. This feature is associated with the ground-state bleaching of the perovskite, whereas the broad positive absorption band spanning 550−720 nm is due to charge carriers generated in the photoexcited material.[48−50] A shift of 6 nm is observed between the negative peaks of the EA and TA spectra with full width at half-maximum (fwhm) values of 20 and 30 nm, respectively. The EDA spectrum recorded 300 ps after pump excitation is also shown in Figure 2. The negative band at 751 nm is slightly blue-shifted relative to the ground-state bleaching observed in the TA spectrum. Whereas a positive band at 680−720 nm is observed, the transient absorption feature due to photogenerated carriers appearing in the TA spectrum at shorter wavelengths ($\lambda_{probe} < 660$ nm) is absent here, because it was subtracted in the calculation of the differential spectrum (eq 3).

The EDA spectra at selected times after pump excitation are shown in Figure 3. At a delay time of ≤0 ps, the pump pulse has not yet generated charge carriers, and therefore, the EDA and steady-state EA spectra are identical. After pump excitation, the photogenerated electrons and holes in the perovskite layer drift toward the oppositely biased electrodes. The carrier separation
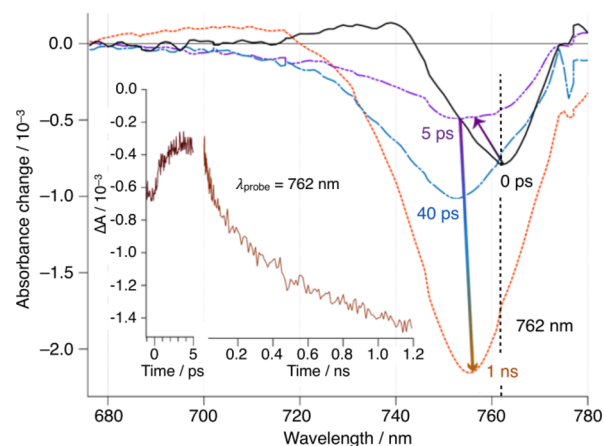
Figure 3. Time evolution of the electromodulated differential absorption (EDA) spectra of insulated MAPbI$_3$ films excited at $\lambda_{pump} = 545$ nm and subjected to an external electric field $|E|_0 = 9.4 \times 10^4$ V cm^{-1} ($U = 6$ V). Inset: Time dependence of the differential absorbance change recorded under the same conditions at $\lambda_{probe} = 762$ nm.

produces a space charge and a transient electric field $\mathbf{E}_s$ that opposes the steady field $\mathbf{E}_0$ applied between the electrodes. It reduces the effective field strength, $|\mathbf{E}_{eff}| = |\mathbf{E}|_0 - |\mathbf{E}_s|$, exerted on the MAPbI$_3$ film and consequently decreases the amplitude of the electroabsorption. The EDA signal dynamics depends on the carriers' drift velocity and, hence, on their mobility. EDA dynamics monitored at the peak of the negative band associated with the Stark shift (see the inset of Figure 3 and Si Figure S4) shows a decrease of the signal amplitude by approximately one-half at early times that can be attributed to the field-induced charge separation and the ensuing screening of the applied electric field exerted on the perovskite film. This initial carrier motion step is completed within 3 ps, at which point the EDA signal flattens out, indicating that there is no further rapid change in the effective field experienced by the material.

On a longer time scale, we observe that, after the initial decrease on the picosecond range, the amplitude of the transient negative signal increases with a half-reaction time of ca. 0.4 ns. The ingrowth in the bleaching band extends far beyond the initial amplitude at time zero resulting from the initially observed Stark effect and is accompanied by a 7–9-nm blue shift. This indicates that the slowly growing negative signal peaking at $\lambda_{probe} = 755$ nm is unrelated to the field-induced Stark shift of the absorption spectrum. This phenomenon, however, is observed only when the external electric field is applied and will be discussed in the following section.

Figure 4 compares TA and EDA signals obtained under similar conditions. Because no charge extraction from the insulated perovskite film is possible, the time evolution of the TA dynamics must result from carrier recombination. In the
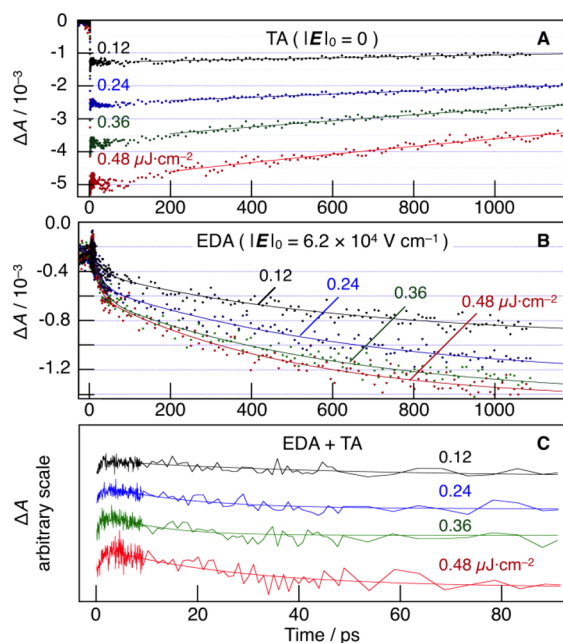
absence of an applied electric field, a decay of the ground-state bleaching is indeed observed, whose kinetics depends on the excitation pulse energy fluence and the resulting initial photogenerated carrier density (Figure 4A). Single-exponential fitting of the recombination dynamics yields time constants of $\tau_r = 5.2, 4.8, 3.4$, and 3.4 ± 0.2 ns for pump energy fluences of $\Psi = 0.12, 0.24, 0.36$, and $0.48 \; \mu J \; cm^{-2}$ per pulse, respectively. The observed pseudo-first-order rate constant $k_r = 1/\tau_r$ does not scale linearly with the initial photocarrier density n_0, which is proportional to the energy fluence Ψ. Because the recombination between carriers, where at least one is free, should be characterized by a second-order rate law ("bimolecular" recombination mechanism), this result suggests that charge recombination in this case proceeds mainly between correlated electron–hole pairs localized in Wannier–Mott excitons or in neighboring trap sites (Shockley–Read–Hall mechanism). The energy fluence per excitation pulse used in our experiments was kept at low values corresponding at most ($\Psi = 0.48 \; \mu J \cdot cm^{-2}$) to 1 Sun (AM1.5G) $\times$ 200 ns and an initial impulsive photocarrier density of $n_0 = 4.2 \times 10^{16} \; cm^{-3}$. This value is likely to be comparable to or less than the trap density within the material, which has been estimated for solution-processed polycrystalline MAPbI$_3$ films to range between 10^{16} and $10^{18} \; cm^{-3}$.[34]

Rather than decaying, the EDA ground-state bleaching signal increases markedly after the initial 5-ps period with apparent biphasic dynamics (Figure 4B). Fitting of the slower kinetic component yields time constants quite similar to those extracted from the TA signals for carrier recombination. When the external electric field is applied, charge migration in opposite directions indeed prevents electron–hole recombination to a large extent. The suppression of the carrier recombination and subsequent ground-state absorption recovery must result in a growing negative differential absorption in the EDA response that mirrors the decay of the TA, in terms of both kinetics and amplitude. This slow contribution is subtracted in Figure 4C by plotting

EDA − (−TA)

$$\Delta A(t, \lambda) = A_{E+pump}(t, \lambda) - A(\lambda) \tag{5}$$

The results reveal a fast kinetic component with a first-order time constant of $\tau = 24 \pm 4$ ps that is decoupled from both the initial signal growth assigned to the screening of the Stark effect at time delays shorter than 5 ps and the slow decay due to carrier recombination on the nanosecond time scale. This 24-ps component is attributed to the migration of carriers and accumulation at the two opposite film surfaces. Further charge separation should screen the electroabsorption more and thus produce an upward absorbance change signal. This contribution, however, is apparently overcompensated here by an increase of the bleaching of the material at the probe wavelengths, which credibly results from a Burstein–Moss blue shift of the absorption threshold.[50,51] Because the two phenomena are characterized by the same time evolution, the combination of their respective signals yields the same kinetic parameter.

A closer look at the sum of the TA and EDA signals (see Figure S6) shows that the recombination dynamics is indeed completely suppressed for initial photocarrier densities of $n_0 \leq 2 \times 10^{16} \; cm^{-3}$. At higher pump energy fluences ($n_0 \geq 3 \times 10^{16} \; cm^{-3}$), however, a residual slow recovery of the ground-state absorption is still observed. This suggests that a portion of the

Figure 4. Subnanosecond time evolution of the transient absorption (TA) and electromodulated differential absorption (EDA) signals recorded for increasing values of the energy fluences at $\lambda_{pump} = 545$ nm. (A) TA dynamics of carrier recombination in the absence of a field. (B) EDA dynamics obtained upon application of an external field of $|\mathbf{E}|_0 = 6.2 \times 10^4 \; V \; cm^{-1}$ ($U = 4.0$ V). (C) EDA dynamics after subtraction of the carrier recombination contribution (eq 5). The vertical positioning of the traces is arbitrary. All measured absorbance changes (TA and EDA) were averaged on the probe wavelength interval 749 nm < λ_{probe} < 757 nm.

more deeply trapped carriers were not separated by the electric field within the first tens of picoseconds and eventually recombined on a nanosecond time scale.

The interpretation of these results is schematized in Figure 5A. Band-gap irradiation of undoped MAPbI$_3$ perovskite at a
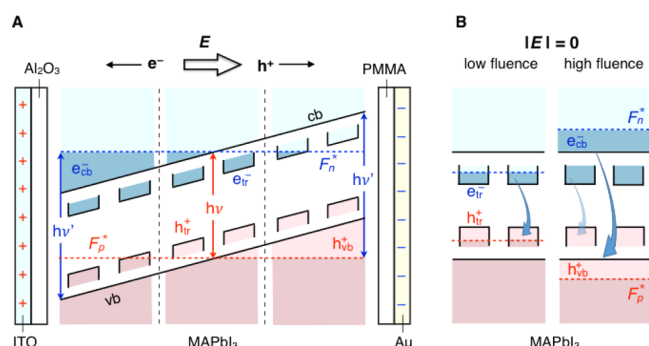

Figure 5. (A) Schematic showing how photogenerated charge carriers can accumulate at both surfaces of an insulated perovskite thin film within an externally applied electric field. Populated electronic states appear in dark blue for the conduction band (cb) and electron traps and dark pink for the valence band (vb) and hole traps. F_n* and F_p* are quasi-Fermi levels for electrons and holes, respectively, in the material under illumination. Accumulation of carriers causes a blue shift ($h\nu'$ > $h\nu$) of the absorption threshold of the material. (B) In the absence of an electric field, free carriers are produced upon irradiation at high irradiation intensity and subsequent filling of trap states. Curved arrows represent electron−hole recombination in trap sites and between free carriers.

pump wavelength of 545 nm generates out-of-equilibrium charge carriers. The application of an external field |**E**|$_0$ quickly separates charges over an initial distance corresponding to the size of crystal grains. Typical dimensions of such domains (see Figure 1) range from 10 to 100 nm. An average value of the grain length in the transverse direction was determined from several cross-sectional SEM images to be d = 40 nm. The initial decay of the electric field exerted on the material, as probed optically by the screening of the electroabsorption response, shows that the initial charge separation takes place with a time constant of τ_1 = 0.94 ± 0.1 ps (see Figure S4). Assuming an average transit time of carriers in individual grains of $l_\pm$ = d/2 = 20 nm, a value of $\mu_\pm$ = $l_\pm/(\tau_1|\mathbf{E}|_0)$ = 22.6 ± 4 cm^2 V^{-1} s^{-1} is inferred for the intragrain carrier drift mobility averaged over electrons and holes (see SI for calculation details).

As the photogenerated charge carriers further migrate toward the oppositely biased electrodes, they accumulate at the interface with insulating layers, forming n- and p-doped regions at the surface of the perovskite film. A Burstein−Moss blue shift of the MAPbI$_3$ absorption spectrum owing to the carriers' accumulation was observed to build up with a time constant τ_2 = 24 ± 4 ps under a bias voltage of 4.0 V. Because the observed Burstein−Moss shift of the absorption edge of the semiconductor can result from the accumulation of only one specific type of carrier (see Figure 5A), the transit time measured in this case must be related to the type of carrier that is the first to reach an interface. Assuming that the accumulation of electrons in MAPbI$_3$ at the proximity of the alumina layer is responsible for the growing in of the bleaching signal, a value for the mobility of the negative charge carriers of μ_n = 5.5 ± 1 cm^2 V^{-1} s^{-1} is calculated. Alternatively, if holes are the first to accumulate at the interface between the perovskite film and PMMA, their mobility would be determined as μ_p = 13.3 ± 2

cm^2 V^{-1} s^{-1} (see SI for calculation details). In the latter hypothesis, the mobility of the electrons, μ_n < 5.5 cm^2 V^{-1} s^{-1}, would be ca. 3 times smaller than that of the holes. Retention of negative carriers in deeper traps could provide a rationale for this difference. However, if the first assumption is true, namely, that electrons are the first to accumulate and cause the bleaching signal, a value of μ_p < 13 cm^2 V^{-1} s^{-1} would be implied, which is compatible with an electron-to-hole mobility ratio of ∼2 ($\mu_p \approx$ 3 cm^2 V^{-1} s^{-1}) determined by terahertz and microwave photoconductivity measurements[52,53] and predicted by computational calculations.[54,55] In both cases, or if a mobility averaged over electrons and holes of $\mu_\pm$ = 9.4 ± 2 cm^2 V^{-1} s^{-1} is considered, one observes that the drift mobility of carriers along their path across the multigrain film is reduced at least by a factor of 2−4 compared to the intragrain, averaged mobility. This indicates the significant limitation of the drift velocity of carriers across the polycrystalline film by scattering at grain boundaries.[27,30]

In the absence of a field (Figure 5B), there is no driving force for charge separation, and photogenerated carriers are annihilated through electron−hole recombination. When the irradiation intensity is low and the trap density is rather significant, a majority of carriers get trapped. Their recombination, then, proceeds mostly through a trap-assisted, geminate mechanism on the nanosecond time scale. In contrast, large carrier densities would be obtained upon strong irradiation. Trap filling occurs in that case, allowing free carriers to recombine with faster, bimolecular dynamics.

In an attempt to discriminate between the respective contributions of electrons and holes, we carried out preliminary EDA measurements of thin films of evaporated MAPbI$_3$ in an architecture that would allow charge extraction at both electrodes. The investigated sample had the alumina insulator replaced by a thin mesoporous nanocrystalline TiO$_2$ layer between the ITO conductive glass substrate and the perovskite. On the cathode side, the PMMA insulating layer was omitted, and gold was evaporated directly on top of the MAPbI$_3$ film. The U = 4.0 V reverse bias applied in this case was expected to make the TiO$_2$ act as an effective electron-transport layer, whereas holes would be readily extracted at the gold electrode. Similarly to the case of the insulated perovskite film, screening of the externally applied electric field by intragrain carrier separation was observed to take place within a few picoseconds (see Figure S9). Following this early decrease of the electroabsorption response, a growing bleaching signal with time constant of ∼20−50 ps was monitored again, which was indicative of carrier accumulation at one or both interfaces. A slow recovery of the ground-state absorption of the perovskite was finally observed with a half-reaction time of $t_{1/2} \approx$ 300 ps. The latter kinetic component was absent in insulated devices and is therefore assigned to the slow injection of accumulated carriers through one of the interfaces. A poor junction between the mesoporous titania and the polycrystalline vapor-deposited perovskite is expected, owing to rather sparse punctual contacts between the TiO$_2$ spherical particles and the nanometer-sized angular grains of the perovskite. On the contrary, the evaporated gold film forms a conformal junction with the active layer. It is, therefore, very likely that the observed carrier accumulation and delayed extraction concerns electrons at the MAPbI$_3$|TiO$_2$ interface.

CONCLUSIONS

The time-resolved electroabsorption spectroscopy (TREAS) technique was successfully applied for the first time to a methylammonium lead triiodide perovskite film. The active material was prepared by vapor deposition and appeared to be polycrystalline with an average grain size of 40 nm. $MAPbI_3$ subjected to an externally applied electric field on the order of 10 MV m^{-1} displayed a blue shift of its excitonic absorption edge at 780 nm, corresponding to a quadratic electroabsorption response compatible with both Stark and Franz–Keldysh–Aspnes models. The electroabsorption signal was exploited to probe optically the time evolution of the local electric field experienced by the perovskite.

Upon band-gap irradiation, electron–hole pairs were formed. Their initial spatial separation was observed from the EDA signal dynamics to take place with a time constant of 0.94 ± 0.1 ps, until charges were trapped at grain boundaries. An average intragrain dc mobility of the carriers of $\mu_\pm = 23 \pm 4$ cm^2 V^{-1} s^{-1} was extracted from this result, in good agreement with terahertz spectroscopy measurements.[53,55–57] A second charge separation step was observed optically with a time constant of 24 ± 4 ps. This kinetic component was assigned to the detrapping of carriers and their migration to the opposite insulated film surfaces, where they accumulated, producing a Burstein–Moss blue shift of the absorption spectrum of the $MAPbI_3$ material. A value of the mobility, limited by trapping–detrapping processes at grain boundaries, of $\mu_n = 5.5 \pm 1$ cm^2 V^{-1} s^{-1} was estimated for electrons drifting across the entire film thickness. Importantly, charge recombination was observed to be entirely suppressed between field-separated carriers generated at initial densities of $n_0 \leq 2 \times 10^{16}$ cm^{-3}.

The TREAS technique also proved quite powerful in characterizing the kinetics of the charge transmission between the perovskite absorber material and the carrier-extracting layers in fully operational photovoltaic devices. In particular, electron accumulation at the junction between the vapor-deposited $MAPbI_3$ film and a mesoporous nanocrystalline TiO_2 layer was observed before the charge extraction could take place at the subnanosecond time scale.

EXPERIMENTAL SECTION

Sample Preparation. An ITO conductive glass substrate was covered by atomic layer deposition (ALD) with a 30-nm-thick film of insulating alumina. Al_2O_3 was deposited from pulses of $Al(CH_3)_3$ precursor and water vapor at 114 °C.[58] A 280-nm-thick film of $MAPbI_3$ was then coated on top of the alumina layer by thermally coevaporating methylammonium iodide (CH_3NH_3I) and lead iodide (PbI_2) in a vacuum. Methylammonium iodide was synthesized and purified following a reported recipe.[59] PbI_2 (99%, Aldrich) was used as received. Substrates and chemicals were loaded in an evaporator chamber (custom-built, Lesker). The chamber was pumped down to a base pressure of 9×10^{-6} mbar. The methylammonium iodide source was contained in a molybdenum boat covered by a perforated lid (Omnicore). The CH_3NH_3I evaporation rate was adjusted with a proportional–integral–derivative (PID) controller conditioning the heating power supply with a pressure set point of 1.23×10^{-4} mbar. PbI_2 was placed in a quartz crucible heated by a tungsten wire coil (EVB9, EVC2, Lesker), and its evaporation rate was controlled with a quartz microbalance placed inside the chamber. The rate of $MAPbI_3$ deposition onto the substrate was 0.03 nm s^{-1}. Details on the evaporation setup and procedure are provided in ref 43. An insulating poly(methyl methacrylate) (PMMA) layer (25–30 nm thick) was deposited by spin-coating on top of the evaporated perovskite. PMMA beads (MW 120000, Sigma-Aldrich) were dissolved in chlorobenzene (15 mg/mL), and the solution was spin-coated (5000 rpm for 2 min) in a glovebox under a dry and oxygen-free atmosphere. Gold was finally thermally evaporated on the polymer (BenchTop Turbo evaporator, Denton), yielding an 80-nm-thick film of metal. Samples were kept in the glovebox until they were used for laser experiments. The aforementioned vacuum deposition techniques were employed to prepare complete solar cell devices with an ITO conductive glass|mesoporous nanocrystalline TiO_2|vapor-deposited $MAPbI_3$|Au architecture. Deposition of the 2-μm-thick mesoporous titania layer was carried out by spin-coating a colloidal solution of TiO_2 with a particle diameter of 20 nm at 5000 rpm for 20 s. The film was then gradually heated to 500 °C and sintered at that temperature for 15 min.

Ultrafast Transient Absorption Spectroscopy Setup. Similar pump–probe schemes were used for ultrafast transient absorption spectroscopy and TREAS measurements. Both experiments were based on a common amplified Ti:sapphire femtosecond laser system (CPA-2001, Clark-MXR), with an output wavelength of 780 nm at a repetition rate of 1 kHz. The pump beam at 545 nm was generated by a two-stage noncollinear optical parametric amplifier (NOPA-Plus, Clark-MXR), with a typical pulse duration of 50–60 fs. The probe beam consisted of a white-light continuum, generated by passing part of the 780-nm laser output through a 5-mm-thick moving CaF_2 plate (for TA, 400–1050 nm) or through a 3-mm-thick sapphire disk (for EDA, 400–750 nm). The remaining fundamental was removed with appropriate filters. The pump and probe pulses were time-delayed with respect to one another using a computerized translation stage, and they were crossed in the sample. The relative polarization of the two beams was at the magic angle. After being transmitted through the TA sample or being reflected off the gold electrode of the EDA sample (which was entered through the transparent ITO layer), the probe beam was dispersed in a grating spectrograph (SpectraPro 2500i, Princeton Instruments or SR163, Andor Technology) and finally detected shot by shot at a 1 kHz rate with a 512 × 58 pixel back-thinned CCD detector (S07030-0906, Hamamatsu). Part of the probe beam was split before the sample into a reference beam reaching a second detector, which allowed for corrections for shot-to-shot fluctuations. For TA spectroscopy, the pump beam was chopped at one-half the amplifier repetition rate (500 Hz). In EDA experiments, each probe pulse was crossed with the pump at the full 1 kHz repetition rate. The voltage applied to the electrodes was modulated at 500 Hz using a function generator (AFG 2021, Tektronix), which provided square voltage pulses (up to 6-V reverse bias, 100-μs pulse duration). Multiple samples were measured under the same conditions, yielding consistent results.

ASSOCIATED CONTENT

Ⓢ Supporting Information

The Supporting Information is available free of charge on the ACS Publications website at DOI: 10.1021/acs.jpcc.6b08022.

Detailed analysis of data, calculation procedures, discussions, and additional figures mentioned in the

text: Absorption spectrum of the perovskite film, calculation of the modulus of the effective external electric field exerted on the MAPbI₃ film, details of intragrain charge dynamics, dependence of the differential electroabsorption signal on the electric field magnitude and pump energy fluence, evaluation of the carrier mobility, and accumulation of electrons at the MAPbI₃|TiO₂ junction (PDF)

■ AUTHOR INFORMATION

Corresponding Author

*E-mail: je.moser@epfl.ch. Phone: +41 21 693 3628.

Notes

The authors declare no competing financial interest.

■ REFERENCES

(1) Kim, H.-S.; Lee, C.-R.; Im, J.-H.; Lee, K.-B.; Moehl, T.; Marchioro, A.; Moon, S.-J.; Humphry-Baker, R.; Yum, J.-H.; Moser, J.-E.; Grätzel, M.; Park, N.-G. Lead Iodide Perovskite Sensitized All-Solid-State Submicron Thin Film Mesoscopic Solar Cell with Efficiency Exceeding 9%. *Sci. Rep.* **2012**, *2*, 591.

(2) Lee, M. M.; Teuscher, J.; Miyasaka, T.; Murakami, T. N.; Snaith, H. J. Efficient Hybrid Solar Cells Based on Meso-Superstructured Organometal Halide Perovskites. *Science* **2012**, *338*, 643−647.

(3) Lin, Q.; Armin, A.; Burn, P. L.; Meredith, P. Organohalide Perovskites for Solar Energy Conversion. *Acc. Chem. Res.* **2016**, *49*, 545−553.

(4) Zhao, Y.; Zhu, K. Organic-Inorganic Hybrid Lead Halide Perovskites for Optoelectronic and Electronic Applications. *Chem. Soc. Rev.* **2016**, *45*, 655−689.

(5) Saliba, M.; Matsui, T.; Seo, J.-Y.; Domanski, K.; Correa-Baena, J.-P.; Nazeeruddin, M. K.; Zakeeruddin, S. M.; Tress, W.; Abate, A.; Hagfeldt, A.; Grätzel, M. Cesium-Containing Triple Cation Perovskite Solar Cells: Improved Stability, Reproducibility and High Efficiency. *Energy Environ. Sci.* **2016**, *9*, 1989−1997.

(6) Burschka, J.; Pellet, N.; Moon, S.-J.; Humphry-Baker, R.; Gao, P.; Nazeeruddin, M. K.; Grätzel, M. Sequential Deposition as a Route to High-Performance Perovskite-Sensitized Solar Cells. *Nature* **2013**, *499*, 316−319.

(7) Liu, M.; Johnston, M. B.; Snaith, H. J. Efficient Planar Heterojunction Perovskite Solar Cells by Vapour Deposition. *Nature* **2013**, *501*, 395−398.

(8) Gamliel, S.; Etgar, L. Organo-Metal Perovskite Based Solar Cells: Sensitized versus Planar Architecture. *RSC Adv.* **2014**, *4*, 29012−29021.

(9) Docampo, P.; Bein, T. A Long-Term View on Perovskite Optoelectronics. *Acc. Chem. Res.* **2016**, *49*, 339−346.

(10) Stranks, S. D.; Eperon, G. E.; Grancini, G.; Menelaou, C.; Alcocer, M. J.; Leijtens, T.; Herz, L. M.; Petrozza, A.; Snaith, H. J. Electron-Hole Diffusion Lengths Exceeding 1 Micrometer in an Organometal Trihalide Perovskite Absorber. *Science* **2013**, *342*, 341−344.

(11) Xing, G.; Mathews, N.; Sun, S.; Lim, S. S.; Lam, Y. M.; Grätzel, M.; Mhaisalkar, S.; Sum, T. C. Long-Range Balanced Electron- and Hole-Transport Lengths in Organic-Inorganic CH₃NH₃PbI₃. *Science* **2013**, *342*, 344−347.

(12) Dong, Q.; Fang, Y.; Shao, Y.; Mulligan, P.; Qiu, J.; Cao, I.; Huang, J. Electron-Hole Diffusion Lengths > 175 μm in Solution-Grown CH₃NH₃PbI₃ Single Crystals. *Science* **2015**, *347*, 967−970.

(13) Johnston, M. B.; Herz, L. M. Hybrid Perovskites for Photovoltaics: Charge-Carrier Recombination, Diffusion, and Radiative Efficiencies. *Acc. Chem. Res.* **2016**, *49*, 146−154.

(14) Berhe, T. A.; Su, W.-N.; Chen, C.-H.; Pan, C.-J.; Cheng, J.-H.; Chen, H.-M.; Tsai, M.-C.; Chen, L.-Y.; Dubale, A. A.; Hwang, B.-J. Organometal Halide Perovskite Solar Cells: Degradation and Stability. *Energy Environ. Sci.* **2016**, *9*, 323−356.

(15) Bi, D.; Gao, P.; Scopelliti, R.; Oveisi, E.; Luo, J.; Grätzel, M.; Hagfeldt, A.; Nazeeruddin, M. K. High-Performance Perovskite Solar Cells with Enhanced Environmental Stability Based on Amphiphile-Modified CH₃NH₃PbI₃. *Adv. Mater.* **2016**, *28*, 2910−2915.

(16) Guarnera, S.; Abate, A.; Zhang, W.; Foster, J. M.; Richardson, G.; Petrozza, A.; Snaith, H. J. Improving the Long-Term Stability of Perovskite Solar Cells with a Porous Al₂O₃ Buffer Layer. *J. Phys. Chem. Lett.* **2015**, *6*, 432−437.

(17) Snaith, H. J.; Abate, A.; Ball, J. M.; Eperon, G. E.; Leijtens, T.; Noel, N. K.; Stranks; Wang, J. T.-W.; Wojciechowski, K.; Zhang, W. Anomalous Hysteresis in Perovskite Solar Cells. *J. Phys. Chem. Lett.* **2014**, *5*, 1511−1515.

(18) Kim, H.-S.; Park, N.-G. Parameters Affecting I-V Hysteresis of CH₃NH₃PbI₃ Perovskite Solar Cells: Effects of Perovskite Crystal Size and Mesoporous TiO₂ Layer. *J. Phys. Chem. Lett.* **2014**, *5*, 2927−2934.

(19) Tress, W.; Marinova; Moehl, T.; Zakeeruddin, S. M.; Nazeeruddin, M. K.; Grätzel, M. Understanding the Rate-dependent J-V Hysteresis, Slow Time Component, and Aging in CH₃NH₃PbI₃ Perovskite Solar Cells: The Role of a Compensated Electric Field. *Energy Environ. Sci.* **2015**, *8*, 995−1004.

(20) Meloni, S.; Moehl, T.; Tress, W.; Franckevičius, M.; Saliba, M.; Lee, Y. H.; Gao, P.; Nazeeruddin, M. K.; Zakeeruddin, S. M.; Röthlisberger, U.; et al. Ionic Polarization-Induced Current-Voltage Hysteresis in CH₃NH₃PbX₃ Perovskite Solar Cells. *Nat. Commun.* **2016**, *7*, 10334.

(21) Yang, T.-Y.; Gregori, G.; Pellet, N.; Grätzel, M.; Maier, J. The Significance of Ion Conduction in a Hybrid Organic−Inorganic Lead-Iodide-Based Perovskite Photosensitizer. *Angew. Chem., Int. Ed.* **2015**, *54*, 7905−7910.

(22) Eames, C.; Frost, J. M.; Barnes, P. R. F.; O'Regan, B. C.; Walsh, A.; Islam, M. S. Ionic Transport in Hybrid Lead Iodide Perovskite Solar Cells. *Nat. Commun.* **2015**, *6*, 7497.

(23) Yuan, Y.; Huang, J. Ion Migration in Organometal Trihalide Perovskite and Its Impact on Photovoltaic Efficiency and Stability. *Acc. Chem. Res.* **2016**, *49*, 286−293.

(24) Kim, J.; Lee, S.-H.; Lee, J.-H.; Hong, K.-H. The Role of Intrinsic Defects in Methylammonium Lead Iodide Perovskite. *J. Phys. Chem. Lett.* **2014**, *5*, 1312−1317.

(25) Du, M. H. Efficient Carrier Transport in Halide Perovskites: Theoretical Perspectives. *J. Mater. Chem. A* **2014**, *2*, 9091−9098.

(26) Azpiroz, J. M.; Mosconi, E.; Bisquert, J.; De Angelis, F. Defect Migration in Methylammonium Lead Iodide and its Role in Perovskite Solar Cell Operation. *Energy Environ. Sci.* **2015**, *8*, 2118−2127.

(27) Stranks, S. D.; Burlakov, V. M.; Leijtens, T.; Ball, J. M.; Goriely, A.; Snaith, H. J. Recombination Kinetics in Organic-Inorganic Perovskites: Excitons, Free Charge, and Subgap States. *Phys. Rev. Appl.* **2014**, *2*, 034007.

(28) Leijtens, T.; Stranks, S. D.; Eperon, G. E.; Lindblad, R.; Johansson, E. M. J.; McPherson, I. J.; Rensmo, H.; Ball, J. M.; Lee, M. M.; Snaith, H. J. Electronic Properties of Meso-Superstructured and Planar Organometal Halide Perovskite Films: Charge Trapping, Photodoping, and Carrier Mobility. *ACS Nano* **2014**, *8*, 7147−7155.

(29) Wang, L.; McCleese, C.; Kovalsky, A.; Zhao, Y.; Burda, C. Femtosecond Time-Resolved Transient Absorption Spectroscopy of CH₃NH₃PbI₃ Perovskite Films: Evidence for Passivation Effect of PbI₂. *J. Am. Chem. Soc.* **2014**, *136*, 12205−12208.

(30) Wu, X.; Trinh, M. T.; Niesner, D.; Zhu, H.; Norman, Z.; Owen, J. S.; Yaffe, O.; Kudisch, B. J.; Zhu, X.-Y. Trap States in Lead Iodide Perovskites. *J. Am. Chem. Soc.* **2015**, *137*, 2089−2096.

(31) deQuilettes, D. W.; Vorpahl, S. M.; Stranks, S. D.; Nagaoka, H.; Eperon, G. E.; Ziffer, M. E.; Snaith, H. J.; Ginger, D. S. Impact of Microstructure on Local Carrier Lifetime in Perovskite Solar Cells. *Science* **2015**, *348*, 683−686.

(32) Katayama, T.; Jinno, A.; Takeuchi, E.; Ito, S.; Endo, M.; Wakamiya, A.; Murata, Y.; Ogomi, Y.; Hayase, S.; Miyasaka, H. Inhomogeneous Deactivation Process with UV Excitation in Submicron Grains of Lead Iodide Perovskite-Based Solar Cell as Revealed by Femtosecond Transient Absorption Microscopy. *Chem. Lett.* **2014**, *43*, 1656−1658.

(33) Guo, Z.; Manser, J. S.; Wan, Y.; Kamat, P. V.; Huang, L. Spatial and Temporal Imaging of Long-Range Charge Transport in Perovskite Thin Films by Ultrafast Microscopy. *Nat. Commun.* **2015**, *6*, 7471.

(34) Draguta, S.; Thakur, S.; Morozov, Y.; Wang, Y.; Manser, J. S.; Kamat, P. V.; Kuno, M. Spatially Non-Uniform Trap State Densities in Solution-Processed Hybrid Perovskite Thin Films. *J. Phys. Chem. Lett.* **2016**, *7*, 715−721.

(35) Salim, T.; Sun, S.; Abe, Y.; Krishna, A.; Grimsdale, A. C.; Lam, Y. M. Perovskite-Based Solar Cells: Impact of Morphology and Device Architecture on Device Performance. *J. Mater. Chem. A* **2015**, *3*, 8943−8969.

(36) Nie, W.; Tsai, H.; Asadpour, R.; Blancon, J.-C.; Neukirch, A. J.; Gupta, G.; Crochet, J. J.; Chhowalla, M.; Tretiak, S.; Alam, M. A.; et al. Solar cells. High-Efficiency Solution-Processed Perovskite Solar Cells with Millimeter-Scale Grains. *Science* **2015**, *347*, 522−525.

(37) Srimath Kandada, A. R.; Petrozza, A. Photophysics of Hybrid Lead Halide Perovskites: The Role of Microstructure. *Acc. Chem. Res.* **2016**, *49*, 536−544.

(38) Chen, Y.; Peng, J.; Su, D.; Chen, X.; Liang, Z. Efficient and Balanced Charge Transport Revealed in Planar Perovskite Solar Cells. *ACS Appl. Mater. Interfaces* **2015**, *7*, 4471−4475.

(39) Shi, D.; Adinolfi, V.; Comin, R.; Yuan, M.; Alarousu, E.; Buin, A.; Chen, Y.; Hoogland, S.; Rothenberger, A.; Katsiev, K.; et al. Low Trap-Density and Long Carrier Diffusion in Organolead Trihalide Perovskite Single Crystals. *Science* **2015**, *347*, 519−522.

(40) Vithanage, D. A.; Devižis, A.; Abramavičius, V.; Infahsaeng, Y.; Abramavičius, D.; MacKenzie, R. C. I.; Keivanidis, P. E.; Yartsev, A.; Hertel, D.; Nelson, J.; Sundström, V.; Gulbinas, V. Visualizing Charge Separation in Bulk Heterojunction Organic Solar Cells. *Nat. Commun.* **2013**, *4*, 2334.

(41) Gelinas, S.; Rao, A.; Kumar, A.; Smith, S. L.; Chin, A. W.; Clark, J.; van der Poll, T. S.; Bazan, G. C.; Friend, R. H. Ultrafast Long-Range Charge Separation in Organic Semiconductor Photovoltaic Diodes. *Science* **2014**, *343*, 512−516.

(42) Devižis, A.; Hertel, D.; Meerholz, K.; Gulbinas, V.; Moser, J.-E. Time-Independent, High Electron Mobility in Thin PC$_{61}$BM Films: Relevance to Organic Photovoltaics. *Org. Electron.* **2014**, *15*, 3729−3734.

(43) Devižis, A.; De Jonghe-Risse, J.; Hany, R.; Nüesch, F. A.; Jenatsch, S.; Gulbinas, V.; Moser, J.-E. Dissociation of Charge Transfer States and Carriers Separation in Bilayer Organic Solar Cells - A Time-Resolved Electroabsorption Spectroscopy Study. *J. Am. Chem. Soc.* **2015**, *137*, 8192−8198.

(44) Teuscher, J.; Ulianov, A.; Müntener, O.; Grätzel, M.; Tetreault, N. Control and Study of the Stoichiometry in Evaporated Perovskite Solar Cells. *ChemSusChem* **2015**, *8*, 3847−3852.

(45) Roiati, V.; Mosconi, E.; Listorti, A.; Colella, S.; Gigli, G.; De Angelis, F. Stark Effect in Perovskite/TiO$_2$ Solar Cells: Evidence of Local Interfacial Order. *Nano Lett.* **2014**, *14*, 2168−2174.

(46) Trinh, M. T.; Wu, X.; Niesner, D.; Zhu, X.-Y. Many-body Interactions in Photo-excited Lead Iodide Perovskite. *J. Mater. Chem. A* **2015**, *3*, 9285−9290.

(47) Ziffer, M. E.; Mohammed, J. C.; Ginger, D. S. Electroabsorption Spectroscopy Measurements of the Exciton Binding Energy, Electron-Hole Reduced Effective Mass, and Band Gap in the Perovskite CH$_3$NH$_3$PbI$_3$. *ACS Photonics* **2016**, *3*, 1060−1068.

(48) Marchioro, A.; Teuscher, J.; Friedrich, D.; Kunst, M.; van de Krol, R.; Moehl, T.; Grätzel, M.; Moser, J.-E Unravelling the Mechanism of Photoinduced Charge Transfer Processes in Lead Iodide Perovskite Solar Cells. *Nat. Photonics* **2014**, *8*, 250−255.

(49) Sum, T. C.; Mathews, N.; Xing, G.; Lim, S. S.; Chong, W. K.; Giovanni, D.; Dewi, H. A. Spectral Features and Charge Dynamics of Lead Halide Perovskites: Origins and Interpretations. *Acc. Chem. Res.* **2016**, *49*, 294−302.

(50) Anand, B.; Sampat, S.; Danilov, E. O.; Peng, W.; Rupich, S. M.; Chabal, Y. J.; Gartstein, Y. N.; Malko, A. V. Broadband Transient Absorption Study of Photoexcitations in Lead Halide Perovskites: Towards a Multiband Picture. *Phys. Rev. B: Condens. Matter Mater. Phys.* **2016**, *93*, 161205.

(51) Manser, J. S.; Kamat, P. V. Band Filling with Free Charge Carriers in Organometal Halide Perovskites. *Nat. Photonics* **2014**, *8*, 737−743.

(52) Ponseca, C. S., Jr.; Savenije, T. J.; Abdellah, M.; Zheng, K.; Yartsev, A.; Pascher, T.; Harlang, T.; Chabera, P.; Pullerits, T.; Stepanov, A.; et al. Organometal Halide Perovskite Solar Cell Materials Rationalized: Ultrafast Charge Generation, High and Microsecond-Long Balanced Mobilities, and Slow Recombination. *J. Am. Chem. Soc.* **2014**, *136*, 5189−5192.

(53) Ponseca, C. S., Jr.; Sundström, V. Revealing the Ultrafast Charge Carrier Dynamics in Organo Metal Halide Perovskite Solar Cell Materials using Time Resolved THz Spectroscopy. *Nanoscale* **2016**, *8*, 6249−6257.

(54) Umari, P.; Mosconi, E.; De Angelis, F. Relativsitic GW Calculations on CH$_3$NH$_3$PbI$_3$ and CH$_3$NH$_3$SnI$_3$ Perovskites for Solar Cell Applications. *Sci. Rep.* **2014**, *4*, 4467.

(55) Chen, Q.; De Marco, N.; Yang, Y.; Song, T.-B.; Chen, C.-C.; Zhao, H.; Hong, Z.; Zhou, H.; Yang, Y. Under the Spotlight: The Organic − Inorganic Hybrid Halide Perovskite for Optoelectronic Applications. *Nano Today* **2015**, *10*, 355−396.

(56) Karakus, M.; Jensen, S. A.; D'Angelo, F.; Turchinovich, D.; Bonn, M.; Cánovas, E. Phonon-Electron Scattering Limits Free Charge Mobility in Methylammonium Lead Iodide Perovskites. *J. Phys. Chem. Lett.* **2015**, *6*, 4991−4996.

(57) Shi, D.; Adinolfi, V.; Comin, R.; Yuan, M.; Alarousu, E.; Buin, A.; Chen, Y.; Hoogland, S.; Rothenberger, A.; Katsiev, K.; et al. Low Trap-State Density and Long Carrier Diffusion in Organolead Trihalide Perovskite Single Crystals. *Science* **2015**, *347*, 519−522.

(58) Tétreault, N.; Heiniger, L. P.; Stefik, M.; Labouchère, P. L.; Arsenault, E.; Nazeeruddin, N. K.; Ozin, G. A.; Grätzel, M. Atomic Layer Deposition for Novel Dye-Sensitized Solar Cells. *ECS Trans.* **2011**, *41*, 303−314.

(59) Im, J.-H.; Lee, C.-R.; Lee, J.-W.; Park, S.-W.; Park, N.-G. 6.5% Efficient Perovskite Quantum-Dot-Sensitized Solar Cell. *Nanoscale* **2011**, *3*, 4088−4093.

Supporting Information

Dynamics of Photocarrier Separation in

MAPbI$_3$ Perovskite Multigrain Films

under a Quasistatic Electric Field

Arun Aby Paraecattil,[†] Jelissa De Jonghe-Risse,[†] Vytenis Pranculis,[†,‡]

*Joël Teuscher,[†] and Jacques-E. Moser *,[†]*

[†] Photochemical Dynamics Group, Institute of Chemical Sciences & Engineering,

and Lausanne Centre for Ultrafast Science (LACUS), École Polytechnique Fédérale

de Lausanne, CH-1015 Lausanne, Switzerland

[‡] Department of Molecular Compounds Physics, Center for Physical Sciences and Technology,

01108 Vilnius, Lithuania.

* Corresponding author. E-mail: je.moser@epfl.ch. Phone +41 21 693 3628.

S1.   Absorption spectrum of insulated, coevaporated, multigrain MAPbI₃ films
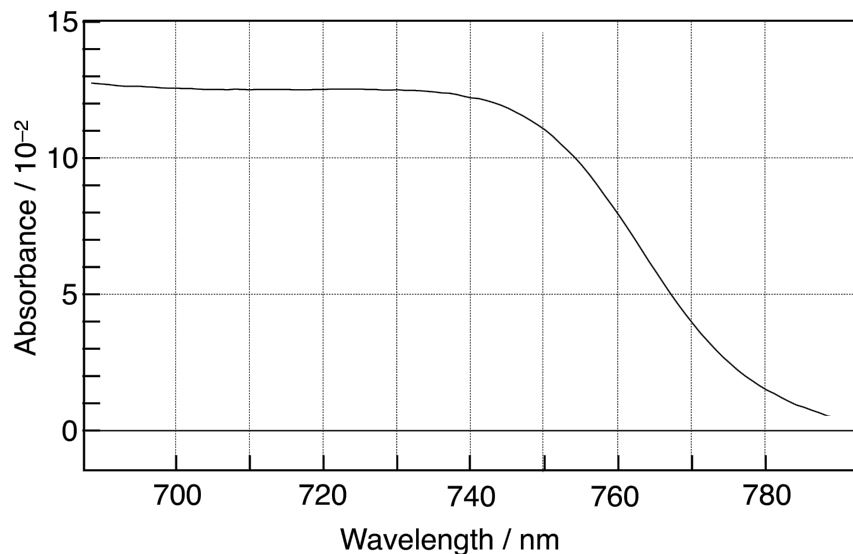
Figure S1. Absorbance spectrum near the absorption edge of a 280-nm-thick vapor-deposited MAPbI$_3$ film sandwiched between alumina and PMMA insulating layers (before thermal evaporation of gold on PMMA). Absorbance between 750 and 790 nm is due primarily to an excitonic absorption band.[1]

S2.   Calculation of the effective external electric field exerted on the MAPbI₃ film

The three-layered insulated perovskite film Al$_2$O$_3$ (30 nm) | MAPbI$_3$ (280 nm) | PMMA (30 nm) can be modelled as three capacitors in series.
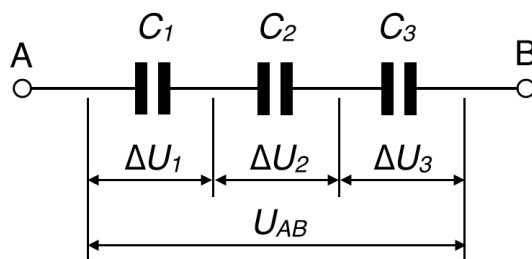
Figure S2. Equivalent circuit of the MAPbI$_3$ film in the dark (C_2), sandwiched between alumina (C_1) and PMMA (C_3) dielectric layers.

Capacitance in a parallel plate capacitor is governed by the following equation:

$$C = \varepsilon_0 \cdot \varepsilon \cdot S / d \tag{S1}$$

where ε_0 is the vacuum permittivity constant, ε the real part of the relative permittivity of the dielectric medium, S the area of the parallel plates and d the distance between them.

The voltage drop ΔU across each capacitor depends on the values of the individual capacitances. By applying Kirchoff's voltage law to the above circuit, it comes :

$$U_{AB} = \Delta U_1 + \Delta U_2 + \Delta U_3 \tag{S2}$$

$$\Delta U_1 = \frac{Q}{C_1} , \; \Delta U_2 = \frac{Q}{C_2}, \; \Delta U_3 = \frac{Q}{C_3} \tag{S3}$$

where Q is the charge stored in each capacitor. Since the total charge stored in the group of three capacitors in series is also Q , one gets :

$$Q = C_{tot} \cdot U_{AB} = C_i \cdot \Delta U_i \tag{S4}$$

$$\frac{1}{C_{tot}} = \frac{U_{AB}}{Q} = \frac{1}{C_1} + \frac{1}{C_2} + \frac{1}{C_3} \tag{S5}$$

$$\Delta U_i = U_{AB} \cdot \frac{C_{tot}}{C_i} = U_{AB} \cdot \frac{1}{C_i} \cdot \frac{1}{\sum_i \frac{1}{C_i}} = U_{AB} \cdot \frac{d_i}{\varepsilon_i} \cdot \frac{1}{\sum_i \frac{d_i}{\varepsilon_i}} \tag{S6}$$

The thickness of each layer was measured by taking several cross-sectional SEM images (see Figure 1), yielding on the average $d_1 = d_3 = 30$ nm and $d_2 = 280$ nm. The relative permittivity of each of the three dielectric materials was more difficult to assess, as a rather broad distribution of values can be found in the literature. MAPbI$_3$ was shown to be characterized by a large (or even 'giant') static relative permittivity, due in particular to ionic movement and molecular dipole contributions from the organic cation.[2, 3] In our case, though, the field is applied in the form of a square pulse voltage for only 100 µs, preventing the slow polarization of the material by ion migration. A moderate isotropic average dielectric constant in the range of 20-30 at a frequency of 10^4-10^5 Hz is believed to better describe the material in conditions prevailing in our experiments. In the following, we will then assume a relative permittivity $\varepsilon_2 = 25$.[3] For ALD-coated alumina, $\varepsilon_1 = 9$ measured at a frequency of 1 MHz was taken from reference.[4] PMMA, like numerous organic solids, has a relative permittivity ranging between 2.5 and 3. A value $\varepsilon_3 = 2.7$, measured at a frequency of 1 MHz, was used for our calculation.[5]

Inserting the above numerical values in equation S6, the voltage drop across the respective Al$_2$O$_3$, perovskite, and PMMA films was calculated as being $\Delta U_1 = 0.13 \cdot U_{AB}$, $\Delta U_2 = 0.44 \cdot U_{AB}$, and $\Delta U_3 = 0.43 \cdot U_{AB}$ (see Figure S3). Hence, for voltage biases $U = 6.0$ V and $U = 4.0$ V applied onto the triple-layer system, the effective external electric field exerted onto the perovskite film in the dark was :

$$|E|_0 = 0.44 \cdot U / d_2 = 0.44 \cdot 6.0 \text{ V} / 280 \times 10^{-7} \text{ cm} = 9.4 \times 10^4 \text{ V cm}^{-1} \quad \text{and}$$

$$|E|_0 = 0.44 \cdot U / d_2 = 0.45 \cdot 4.0 \text{ V} / 280 \times 10^{-7} \text{ cm} = 6.2 \times 10^4 \text{ V cm}^{-1} \text{, respectively.}$$
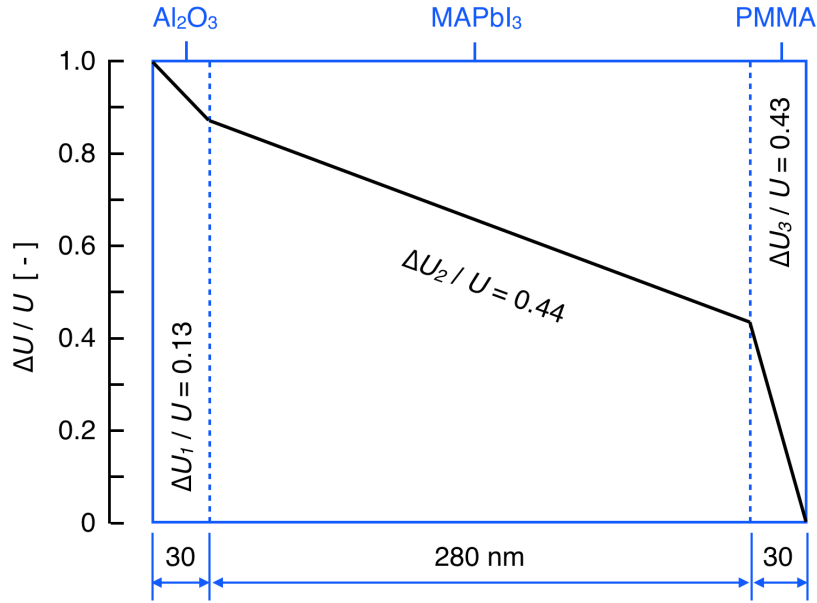
Figure S3. Voltage drop $\Delta U_i / U$ in each dielectric layer, calculated from eq S6 with $\varepsilon_1 = 9$, $d_1 = 30$ nm, $\varepsilon_2 = 25$, $d_2 = 280$ nm, $\varepsilon_3 = 2.7$, and $d_3 = 30$ nm.

It must be noted that the insulating layers, although quite thin, are responsible for the attenuation of more than half of the magnitude of the externally applied electric field, due in particular to the low dielectric permittivity of the PMMA film.

S3. Intragrain charge separation dynamics

The time-evolution of the magnitude of the electric field exerted on the perovskite film, as probed optically by the decay of the electroabsorption response, is shown by the inset of Figure 3. A blow-up of the recorded signal at short time scale is displayed here in Figure S4. Experimental points are found to be fitted quite well by a single exponential function, yielding a time constant $\tau = 0.94 \pm 0.1$ ps.
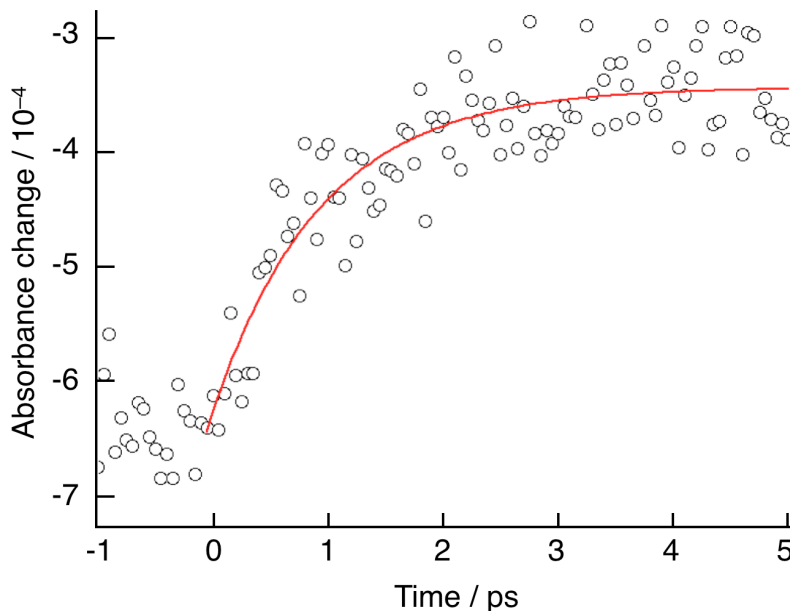
Figure S4. Time-evolution of the electromodulated differential absorbance (EDA) signal recorded at $\lambda_{probe} = 765$ nm for a MAPbI$_3$ perovskite film submitted to an external electric field $|E|_0 = 9.4 \times 10^4$ V cm^{-1} upon ultrashort pulse irradiation at $\lambda_{pump} = 545$ nm. The red line drawn through the experimental points is the result of an exponential fit.

Excitation of MAPbI$_3$ at $\lambda = 545$ nm, far from the excitonic band at the absorption edge of the material, ensures that free carriers are generated during the pump pulse. Screening of the electroabsorption within the first picoseconds, therefore, cannot be assigned to the dissociation of an exciton but results from the drift of electrons and holes in opposite directions until they get trapped at the grain boundaries.

S4.   EDA dependence upon the electric field magnitude and the pump energy fluence

The dynamics of the electromodulated differential absorption (EDA) signals on a long time scale were measured under increasing electric field magnitudes (Figure S5). A double exponential fitting of the experimental points yielded time constants $\tau_2 = 24 \pm 4$ ps and $\tau_r = 500 \pm 12$ ps, independent of the applied bias voltage. The faster part is due to the Burstein-Moss shift of the material upon carrier accumulation at the surfaces, while the slower component, characterized by the time constant τ_r, is a consequence of the prevention of carrier recombination by the application of the external electric field.
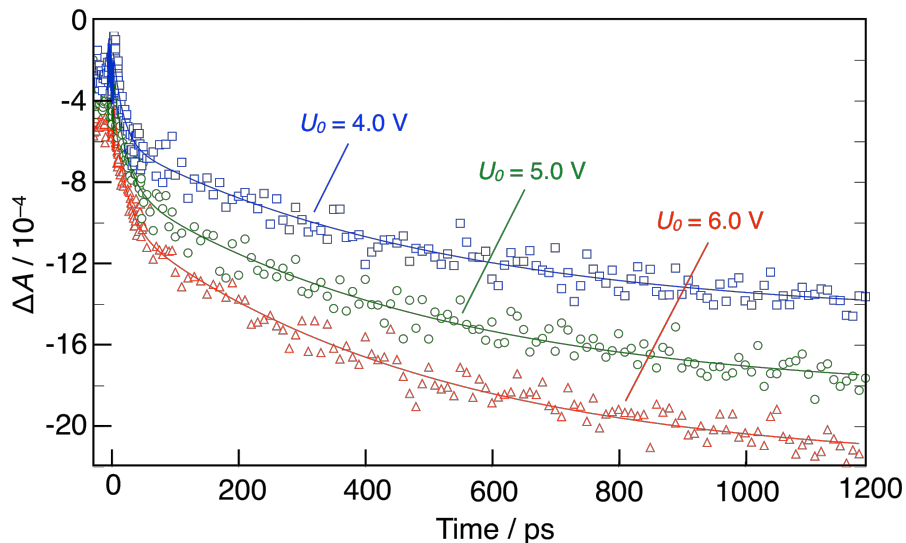
Figure S5. Time-evolution of EDA recorded for increasing values of the applied voltage U_0. Measured absorbance changes were averaged on a probe wavelength interval 749 nm $\leq \lambda_{probe} \leq$ 757 nm. The pump excitation was at $\lambda_{exc.} = 545$ nm, with a constant energy fluence 0.48 μJ cm^{-2}. Continuous curves drawn through experimental points are the result of the fit of a double exponential function.

Figure S6 displays the dependence of the summation of the electromodulated differential absorption (EDA) and transient absorption (TA) signals $\Delta A = \Delta A$ (EDA) − { −ΔA (TA) } upon the pump energy fluence. The slow dynamics observed in Figure S5 with $\tau_r = 500$ ps is only partially perceptible at high fluences, showing that the carrier recombination is entirely suppressed for $n_0 \leq 2\times10^{16}$ cm^{-3}.
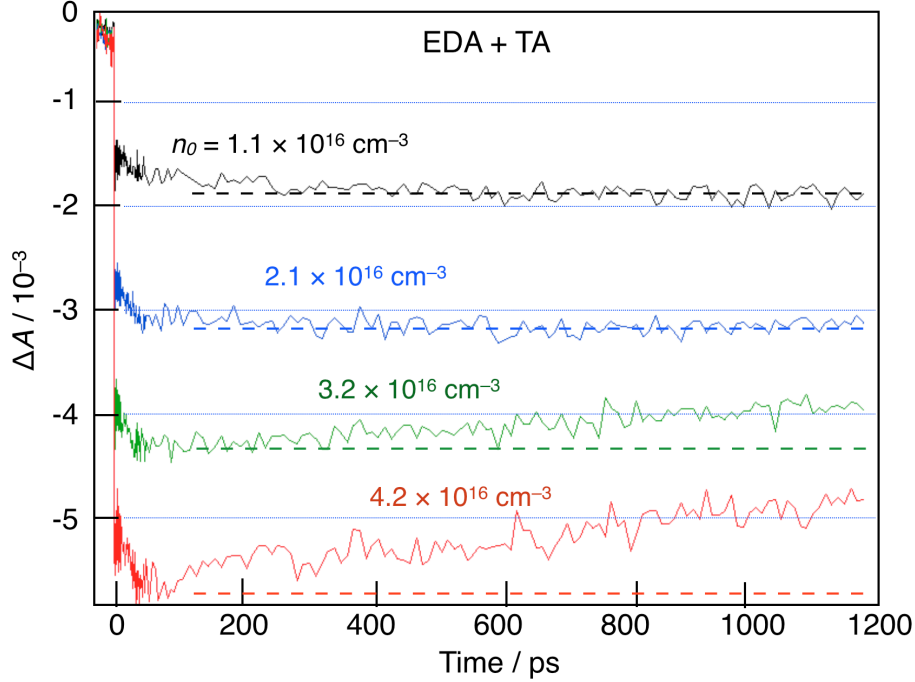
Figure S6. Summation of the electromodulated differential absorption (EDA, $U_0 = 4.0$ V) and transient absorption (TA) signals recorded for increasing values of the pump energy fluences. Labels above the traces correspond to the initial photocarrier densities n_0 achieved by each pump pulse. All measured absorbance changes (TA and EDA) were averaged on a probe wavelength interval 749 nm $\leq \lambda_{probe} \leq$ 757 nm.

S5. Evaluation of the carrier drift mobility

The mobility μ of a charged particle migrating in an electric field is defined by:

$$\mu = v / |\boldsymbol{E}|_0 \tag{S7}$$

where v is the drift velocity of the particle and $|\boldsymbol{E}|_0$ the electric field modulus. The drift velocity $v = l / \tau$ could in principle be estimated directly from the average transit distance l and time τ.

Absorbance changes resulting from the screening of the quadratic Stark effect by drifting charges or from the Burstein-Moss shift induced by the accumulation of carriers at the interfaces were shown to scale linearly with the pump energy fluence (see Figure S6). The time evolution of ΔA signals should then reflect the rate at which carriers reach the boundaries of the grain or of the entire film they moved across. The carrier transit time is spread by the initial spatial distribution of the carriers, as well as by possible dispersive transport and charge trapping processes. Figures S4 and 4C showed that the transient absorbance signal could be fitted in both cases by a single exponential of the form $\Delta A = b \cdot \exp(-kt) + c$, from which an average carrier

transit time $\tau_l = 1 / k$ was estimated. Assuming that the drift velocity is constant, $v = l / \tau$ can be calculated, provided a reasonnably accurate average transit distance l is evaluated.

<u>Evaluation of the average transit distance of carriers</u>

Contrary to the conventional time-of-flight method, where the penetration depth of the pump light is generally small compared to the thickness of the sample and the initial photocarrier distribution can be considered as a quasi-two-dimensional sheet, the extended absorption profile within the perovskite material results in an initial gradient of carrier concentration in the depth of the irradiated film.The average transit distance for electrons and holes can be estimated from the coordinate of the center of mass of carriers generated by the excitation laser pulse.

Let us consider a film of perovskite of thickness L, irradiated through the ITO glass substrate and the Al_2O_3 insulating layer from the left (Figure S7 A). The light transmittance profile across the material is given by the Lambert's law :

$$I(x) = I_0 \cdot \exp(-\alpha x) \tag{S8}$$

where $I(x)$ is the light intensity transmitted at a depth x and α the absorption constant of the material. The density of carriers $dn(x)$ photogenerated within a slice of infinitesimal thickness dx between the coordinates x and $x + dx$ can be written :

$$dn(x) = I(x) - I(x + dx) = I(x) \cdot \left[1 - \exp(-\alpha \cdot dx)\right] \tag{S9}$$

The latter expression can be simplified by using the first two terms of the Maclaurin series expansion :

$$\exp(-\alpha \cdot dx) \approx 1 - \alpha \cdot dx \Rightarrow dn(x) = I(x) \cdot \alpha \cdot dx \tag{S10}$$

Applying again the Lambert's law, the carrier density at the coordinate x can be expressed by :

$$dn(x) = \alpha \cdot I_0 \cdot \exp(-\alpha x) \, dx \tag{S11}$$

The abscissa $\bar{x}$ of the center of mass of photogenerated carriers is finally provided by the expression :

$$\bar{x} = \frac{\int_0^L x \cdot \exp(-\alpha x) dx}{\int_0^L \exp(-\alpha x) dx} = \frac{\frac{1}{\alpha} - \left(L + \frac{1}{\alpha}\right) \cdot \exp(-\alpha L)}{1 - \exp(-\alpha L)} \tag{S12}$$

An absorption constant $\alpha = 6.4 \times 10^4$ cm^{-1} at $\lambda = 545$ nm was obtained from the measured transmittance spectrum of a film of MAPbI$_3$ of known thickness deposited on a quartz substrate. Using the latter value and $L = 280$ nm, the abscissa of the center of mass of the carriers initially

generated by light in the perovskite is determined from eq S12 as being $\bar{x}$ = 82 nm. The average transit distance of electrons to the interface with Al_2O_3, therefore, is $l_n = \bar{x} - 0 = 82$ nm, while that of holes to the interface with PMMA is $l_p = L - \bar{x}$ = 198 nm (Figure S7 B).
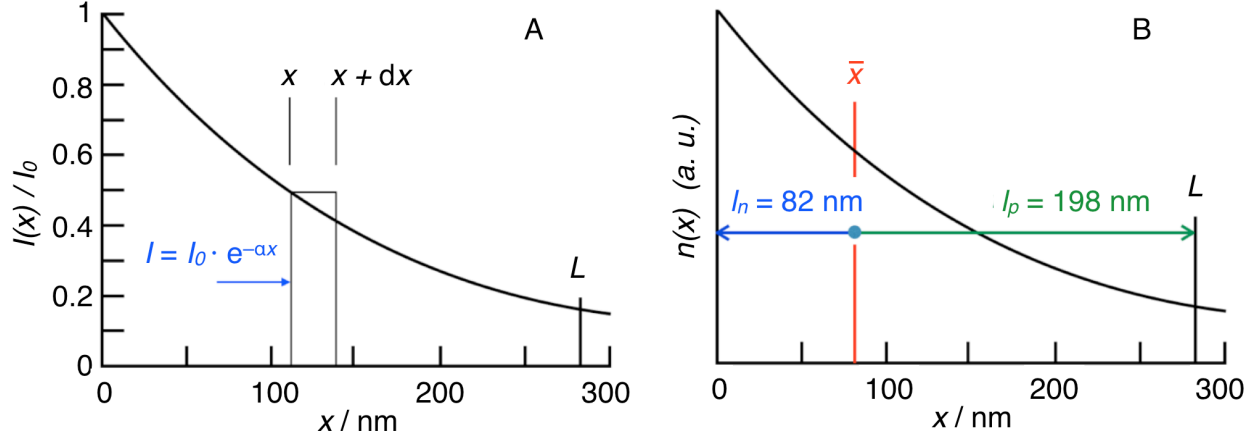

Figure S7. A) Calculated light transmittance profile of a 280 nm-thick $MAPbI_3$ film with α = 6.4×10^4 cm^{-1} at λ = 545 nm. B) The abscissa of the center of mass of photogenerated carriers yielded by eq S12 is $\bar{x}$ = 82 nm.
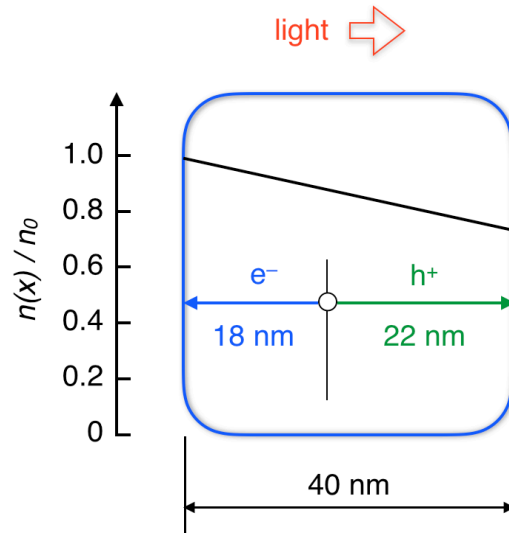

Figure S8. Carrier density profile within a 40-nm $MAPbI_3$ crystal grain irradiated from the left with $\alpha = 6.4 \times 10^4$ cm^{-1}. The calculated average transit distance of electrons to the grain's surface is l_e = 18 nm, while that of holes is l_h = 22 nm.

The initial drift of charge carriers upon ultrafast pulsed photogeneration takes place within individual crystal grains of the perovskite film, whose average length in the transverse direction is 40 nm. Using again $\alpha = 6.4\times10^4$ cm^{-1} at $\lambda = 545$ nm, the light transmittance of one grain is found to be 0.77. Equation S12 returns an average transit distance for electrons and holes to the grain boundaries of 18 nm and 22 nm, respectively (Figure S8).

Evaluation of the carrier drift mobility

A time constant $\tau = 0.94$ ps was determined for intragrain carrier separation under a reverse bias $U = 6.0$ V. On the average, this corresponds to the time necessary for photogenerated carriers to reach the grain boundaries from a position corresponding to their center of mass. Since there is no way to distinguish between electrons and holes, the transit distance to be used in the calculation of the drift velocity must be averaged over negative and positive charge carriers: $l_{\pm} = (l_n + l_p) / 2 = 20$ nm, leading to a drift velocity $v_{\pm} = l_{\pm} / \tau = 2.13\times10^6$ cm s^{-1} and an intragrain average mobility $\mu_{\pm} = v_{\pm} / |E|_0 = 22.6$ cm^2 V^{-1} cm^{-1}. A relative uncertainty of the order of 10 % is estimated for the magnitude of the electric field and at most of 20% for the drift velocity. Consequently, the determined value of $\mu_{\pm}$ is marred by a maximum absolute error of ± 4 cm^2 V^{-1} cm^{-1}.

The increase of the signal owing to the accumulation of carriers at the surface of the perovskite film was characterized by a time constant $\tau = 24 \pm 4$ ps under a bias voltage $U = 4.0$ V. Since the Burstein-Moss shift of the absorption edge of the semiconductor can result from the accumulation of only one specific type of carrier, the transit time measured in this case must be related to the type of carrier being first to reach an interface. Assuming that the accumulation of electrons at the interface between MAPbI$_3$ and alumina is responsible for the bleaching signal, a value of the mobility $\mu_n = l_n / (\tau |E|_0) = 5.5$ cm^2 V^{-1} s^{-1} is calculated. In the hypothesis of holes being first to accumulate at the interface between the perovskite film and PMMA, their mobility would be $\mu_p = l_p / (\tau |E|_0) = 13.3$ cm^2 V^{-1} s^{-1}. Alternatively, a value of the carrier drift mobility averaged over electrons and holes could be considered: $\mu_{\pm} = (\mu_n + \mu_p) / 2 = L / (2\tau |E|_0) = 9.4$ cm^2 V^{-1} s^{-1}. Again, a maximum relative uncertainty of 20% should be taken into account for the latter values.

S6.   Accumulation of electrons at the MAPbI$_3$ | mp TiO$_2$ junction

Here, the investigated sample had the alumina insulator replaced by a thin mesoporous nanocrystalline TiO$_2$ layer between the ITO conductive glass substrate and the perovskite. On the cathode side, the PMMA layer was omitted and gold evaporated directly on top of the MAPbI$_3$ film. The reverse bias $U = 4.0$ V applied in this case is expected to make the TiO$_2$ act as an effective electron transport layer, while holes are readily extracted at the gold electrode. Following the early decay of the Stark effect, a growing bleaching signal with ~20-50 ps time-constant is monitored, which is indicative of carrier accumulation of electrons at the perovskite | TiO$_2$ interface (Figure S9).
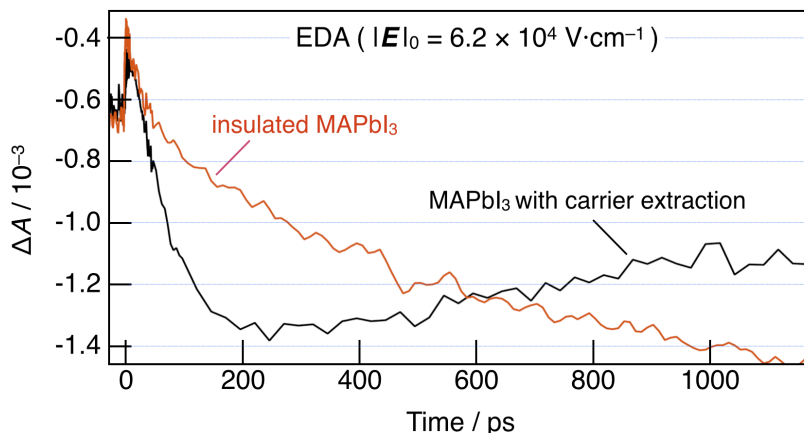
Figure S9. Sub-nanosecond time-evolution of the electromodulated differential absorption (EDA) dynamics obtained upon application of an external electric field $|E|_0 = 6.2 \times 10^4$ V· cm^{-1} ($U = 4.0$ V, reverse bias) on an insulated MAPbI$_3$ perovskite film (red trace) and a solar cell constituted of the same material in contact with a mesoporous TiO$_2$ layer on one side and evaporated gold on the other side (black trace).

S7.   References

(1) Cadelano, M.; Saba, M.; Setsu, N.; Sarritzu, V.; Marongiu, D.; Chen, F.; Piras, R.; Quochi, F.; Mura, A., Bongiovanni, G. Photoexcitation and Emission Processes in Organometal Trihalide Perovskites, in "Perovskite Materials – Synthesis, Charcterization, Properties, and Applications", Pan, L.; Zhu, G. (Eds.), InTech, **2016** (DOI: 10.5772/60469).

(2) Lin, Q.; Armin, A.; Nagiri, R. C. R.; Burn, P. L.; Meredith, P. Electro-Optics of Perovskite Solar Cells. *Nat. Photon.*, **2014**, *9*, 106-112.

(3) Juarez-Perez, E. J.; Sanchez, R. S.; Badia, L.; Garcia-Belmonte, G.; Kang, Y. S.; Mora-Sero, I.; Bisquert, J. Photoinduced Giant Dielectric Constant in Lead Halide Perovskite Solar Cells. *J. Phys. Chem. Lett.*, **2014**, *5*, 2390-2394.

(4) Tanner, C. M.; Perng, Y. C.; Frewin, C.; Saddow, S. E.; Chang, J. P. Electrical Performance of Al$_2$O$_3$ Gate Dielectric Films Deposited by Atomic Layer Deposition on 4H-SiC. *Appl. Phys. Lett.*, **2007**, *91*, 203510.

(5) Chandar Sekar, B.; Sathish, S.; Sengoden, R. Spin Coated Nano Scale PMMA Films for Organic Thin Film Transistors. *Phys. Procedia*, **2013**, *49*, 145-157.